Exploration of a systems and control approach to reduce propeller cavitation in a seaway

Vrijdag, Arthur; Schuttevaer, Daan

Important note
To cite this publication, please use the final published version (if applicable).
Please check the document version above.

Exploration of a systems and control approach to reduce propeller cavitation in a seaway

A. Vrijdag[*], D. Schuttevaer

Delft University of Technology, Faculty of Mechanical, Maritime and Materials Engineering, Mekelweg 2, 2628CD, Delft, the Netherlands

ABSTRACT

Dramatic increases in the underwater acoustic signature of ships have been observed during full scale trials in a seaway, compared to calm water conditions. The observed behaviour can be explained by the interaction of waves, wake field and ship propulsion system dynamics in combination with rudder action and ship motions. This paper explores whether a propulsion control system can increase the cavitation free time when sailing a straight course in a seaway. While in the past non-linear simulation tools have been used to analyse propeller cavitation in a seaway, the original contribution of this paper is that it considers the problem from a systems and control point of view. It is shown that the objective of significantly increasing the cavitation free time while simultaneously preventing thermal overloading of the diesel engine cannot simply be met by adjusting engine speed governor settings. It is however concluded that the developed plant and disturbance model are promising tools for advanced controller development and tuning aiming to reduce underwater acoustic signature.

1. Introduction

Acoustic signature management is of importance for naval ships and serves multiple goals: First of all, the risk of being detected by acoustic sensors of the opponent greatly depends on the own acoustic signature. Secondly, the own acoustic detection range is decreased by self-noise, which increases the chance of *being* detected before *having* detected. Besides the relevance for naval ships, the acoustic underwater signature of commercial ships is receiving increased attention due to its effect on wildlife, especially in sensitive areas such as the Arctic (Tyack (2008); Rolland et al. (2012)).

Operational conditions such as wind, waves, ship motions and manoeuvres can have a considerable adverse effect on the acoustic signature of ships because of the earlier onset of cavitation on the propellers caused by the disturbances of ship resistance and propeller wake field. Wake field disturbances for instance cause spatial and temporal variations of angles of attack of the propeller blade sections, resulting in higher likelihood of cavitation inception compared to calm water conditions.

Dramatic decreases in cavitation inception speed were observed during full scale cavitation trials with the hydrographic research vessel HNLMS Tydeman (Verkuyl and van Terwisga, 2000). This paper in particular shows the observed change in cavitation inception speed when sailing different headings with respect to the waves and secondly

shows the effect of rudder angle on the cavitation inception speed. The effect of a turning manoeuvre on cavitation inception is investigated by Kuiper et al. (2002).

The observed decrease in cavitation inception speed of HNLMS Tydeman sailing in waves can qualitatively be explained by Aalbers and van Gent (1984), who show that when sailing in waves the mean angle of attack of a typical propeller blade section becomes higher and shows larger variations than in calm water. Furthermore they show that in view of the width of the cavitation free operating area, it seems impossible to avoid cavitation completely when sailing in waves. They do however state that by adapting the design of the propeller to the wave conditions, the cavitation performance can strongly be influenced.

A number of years later Kuiper and Jessup (1993) show how, by special consideration for blade section design, it is possible to increase the propeller cavitation inception speed, taking into account the variations of sectional inflow due to the calm water wake field. Wave induced wake field variations were however not taken into account.

Jessup and Wang (1996) show the effect of added resistance on the ship operating line in the cavitation diagram. Besides the effect of increased resistance they also consider the effect of the four wake fields that are considered the most 'extreme' from cavitation inception viewpoint. This is done by focussing on those combinations of axial and tangential wake field velocity components that result in the highest and lowest extremes in angle of attack of the blade sections.

The results of a research project focussing on cavitation in operational conditions are published by van Terwisga et al. (2004). By coupling a model of the shaft speed dynamics including simplified diesel engine and controller with a lifting surface propeller analysis code and a wake field model, it was possible to investigate the effect of propulsion control algorithms on propeller cavitation inception in a seaway. It was shown that control algorithms different from the normally applied constant engine speed control have potential to increase the cavitation free time when sailing in waves.

Inspired by simulation results presented by van Terwisga (2000), Vrijdag et al. (2009, 2010) showed that, by actively controlling the effective angle of attack of the propeller blades during ship accelerations and decelerations, the cavitation behaviour could significantly be improved. This was confirmed by full scale implementation of an experimental propulsion control system on board a multi-purpose frigate of the Royal Netherlands Navy. Although attempts were made, the potential of intelligent control for improved cavitation behaviour when sailing in waves was not demonstrated satisfactory. A possible explanation for this is the limited bandwidth and even time-variant behaviour of a conventional hydraulic pitch actuation system (Bakker et al., 2006; Wesselink et al., 2006; Godjevac, 2009; Martelli et al., 2014). To further investigate the potential and limitations of propulsion control with respect to propeller cavitation in waves, the dynamic behaviour of the ship propulsion plant needs to be thoroughly understood.

In Stapersma and Vrijdag (2017), a ship propulsion system model was linearised and its frequency domain characteristics were investigated. Vrijdag and Stapersma (2017) extended this linearised model and used it to analyse the dynamic behaviour of the engine operating point in a seaway. It was shown how this behaviour is dependent on the wave disturbance frequency and on the ship propulsion system characteristics including the settings of the engine speed governor.

In this paper, the linearised model is further extended so that, besides the analysis of behaviour of the engine operating point in the engine envelope, additionally it can be used for analysis of the behaviour of the propeller operating point in the propeller cavitation diagram. The extended linear model is verified by comparison of its behaviour with a non-linear model. Thereafter the effect of different wave encounter frequencies is shown. Finally the possibilities of modifying the system behaviour in regular seaways by changing engine speed governor gain settings are explored. The latter is shown to have an effect on the cavitation inception speed of a ship sailing in a seaway.

The approach taken in this paper differs from earlier research in the sense that use is made of control theory to analyse the system behaviour. The results presented here pave the way towards development and application of more advanced propulsion control.

2. Non-linear and linear simulation model

The non-linear system model used in this paper is based on Vrijdag and Stapersma (2017). Without repeating all model equations, a general overview is given here. The shaft speed dynamics are described by:

$$2\pi \cdot I_p \cdot \frac{dn}{dt} = M_s - M_{prop} \tag{1}$$

in which the total inertia of the drive train (including the added mass of the propeller's entrained water) denoted by I_p, is assumed constant. The ship speed dynamics are modelled as:

$$m_{ship} \cdot \frac{dv_s}{dt} = F_{prop} - F_{ship} \tag{2}$$

in which m_{ship} is the total ship mass including the added mass and is assumed constant. The propeller thrust and torque are modelled based on the open water diagram of the propeller under consideration:
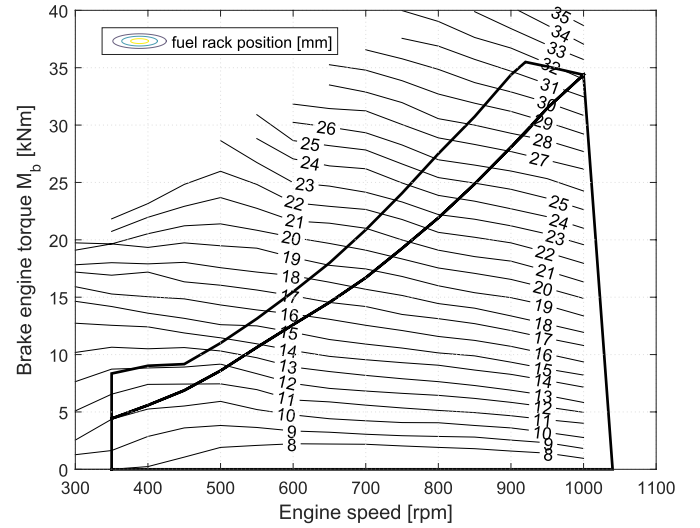

Fig. 1. Engine fuel rack map.

$$T = \rho \cdot n^2 \cdot D^4 \cdot K_T(J, \theta)$$
$$Q = \rho \cdot n^2 \cdot D^5 \cdot K_Q(J, \theta)$$
$$J = \frac{v_s(1-w)}{n \cdot D} \tag{3}$$

The delivered engine torque is based on a static performance map of the engine as shown in Fig. 1.

The fuel rack position X is an output of the (PI) engine speed governor model, which includes an engine speed dependent fuel rack limitation to prevent overloading of the engine. The hydraulic pitch actuation mechanism is strongly simplified and modelled as a first order system, thereby neglecting important non-linearities and time variance that are present, which remains a weak point of the linearised model.

In Vrijdag and Stapersma (2017) a linearised model of both the uncontrolled plant (including actuators) and of a controlled ship propulsion system as shown in Fig. 2 are derived. The actuated uncontrolled model is taken as a basis for further development in this paper.

The general state-space model of the uncontrolled system including actuators is given by:

$$\dot{\mathbf{x}} = A\mathbf{x} + B\mathbf{u} + G\mathbf{w}$$

$$\mathbf{y} = C\mathbf{x} + D\mathbf{u} + H\mathbf{w}$$

with:

$$A = \begin{bmatrix} \frac{(b+g-2)}{\tau_n} & \frac{-b}{\tau_n} & \frac{-q}{\tau_n} \\ \frac{(2-a)}{\tau_v} & \frac{(a-e)}{\tau_v} & \frac{p}{\tau_v} \\ 0 & 0 & \frac{-1}{\tau_\theta} \end{bmatrix}, \quad \mathbf{x} = \begin{bmatrix} \delta n^* \\ \delta v_s^* \\ \delta \theta^* \end{bmatrix}$$

$$B = \begin{bmatrix} \frac{v}{\tau_n} & 0 \\ 0 & 0 \\ 0 & \frac{1}{\tau_\theta} \end{bmatrix}, \quad \mathbf{u} = \begin{bmatrix} \delta X_{set}^* \\ \delta \theta_{set}^* \end{bmatrix}$$

$$G = \begin{bmatrix} 0 & \frac{b}{\tau_n} \\ \frac{-1}{\tau_v} & \frac{-a}{\tau_v} \\ 0 & 0 \end{bmatrix}, \quad \mathbf{w} = \begin{bmatrix} \delta \alpha^* \\ \delta w^* \end{bmatrix}$$

$$\mathbf{y} = \begin{bmatrix} \delta n^* \\ \delta v_s^* \\ \delta \theta^* \\ \delta M_b^* \end{bmatrix}, \quad C = \begin{bmatrix} 1 & 0 & 0 \\ 0 & 1 & 0 \\ 0 & 0 & 1 \\ g & 0 & 0 \end{bmatrix}, \quad D = \begin{bmatrix} 0 & 0 \\ 0 & 0 \\ 0 & 0 \\ v & 0 \end{bmatrix} \tag{4}$$

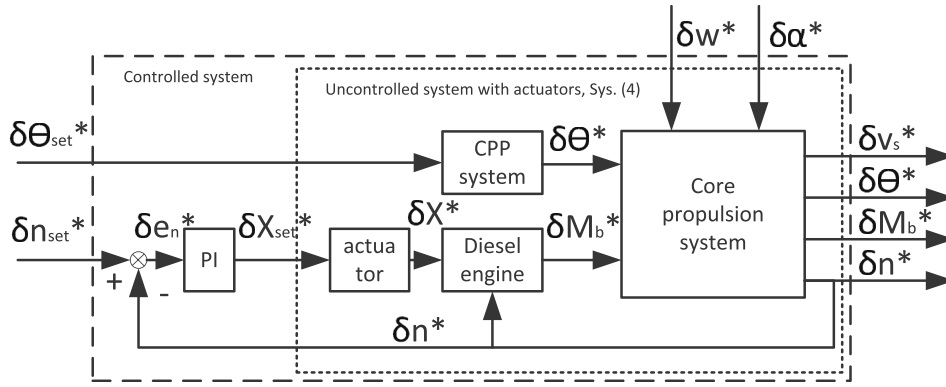This model gives the relation between the three state variables

Fig. 2. Schematic ship propulsion system including the engine speed governor.

engine speed δn^*, ship speed δv_s^* and propeller pitch $\delta \theta^*$, and the inputs propeller pitch setpoint $\delta \theta_{set}^*$, fuel rack setpoint δX_{set}^*, ship resistance disturbance $\delta \alpha^*$ and wake disturbance δw^*. Note that besides all three system states, the brake engine torque δM_b^* is appended as an output.

For reference the definitions of the constants τ_n and τ_v, resistance curve steepness e, propeller derivatives a, b, p and q and diesel engine derivatives g and v are given by:

$$\tau_n \equiv \frac{2\pi \cdot I_p \cdot n_0}{M_{s,0}}, \quad \tau_v \equiv \frac{m_{ship} \cdot v_{s,0}}{F_{ship,0}}, \quad e \equiv \frac{v_{s,0}}{R_0} \cdot \frac{\delta R}{\delta v_s}\Big|_\alpha$$

$$a \equiv \frac{J_0}{K_{T,0}} \cdot \frac{\delta K_T}{\delta J}\Big|_\theta, \quad b \equiv \frac{J_0}{K_{Q,0}} \cdot \frac{\delta K_Q}{\delta J}\Big|_\theta$$

$$p \equiv \frac{\theta_0}{K_{T,0}} \cdot \frac{\delta K_T}{\delta \theta}\Big|_J, \quad q \equiv \frac{\theta_0}{K_{Q,0}} \cdot \frac{\delta K_Q}{\delta \theta}\Big|_J,$$

$$g \equiv \frac{n_0}{M_{b,0}} \cdot \frac{\delta M_b}{\delta n}\Big|_X, \quad v \equiv \frac{X_0}{M_{b,0}} \cdot \frac{\delta M_b}{\delta X}\Big|_n \tag{5}$$

The parameter τ_θ is the time constant of the pitch actuation system. The PI engine speed governor that was implemented in Vrijdag and Stapersma (2017) is defined by:

$$\delta X_{set}^* = K_p \delta e_n^* + K_i \delta E_n^* \tag{6}$$

where the error in engine speed is defined as:

$$\delta e_n^* = \delta n_{set}^* - \delta n^* \tag{7}$$

and the integral of the error is given by:

$$\delta E_n^* = \int_0^t \delta e_n^* dt \Rightarrow \frac{dE_n^*}{dt} = \delta e_n^* \tag{8}$$

The parameters K_p and K_i are the proportional and integral gains of the engine speed governor. For a more detailed treatment of the linearised model including its verification, reference is made to Stapersma and Vrijdag (2017) and Vrijdag and Stapersma (2017).

3. Model extensions

In this paper three main additions are made to the linear model of the ship propulsion plant:

1. The propeller thrust coefficient K_T is added as an output.
2. The cavitation number σ_n is linearised as a function of the sea surface elevation at the location of the propeller and the shaft speed, and added as an output.
3. The wake disturbance is written as a linear function of the sea surface elevation at the location of the propeller so that the latter can be used as a system disturbance input.

As both the cavitation number and wake disturbance are a function of the sea surface elevation at the location of the propeller, they are correlated. The aforementioned additions give the possibility to investigate the behaviour of the propeller operating point in the cavitation diagram, alongside the behaviour of the engine operating point in the engine envelope.

3.1. The thrust coefficient K_T

The traditional propeller cavitation bucket is often presented in a plane spun by the propeller thrust coefficient and the cavitation number. The instantaneous thrust coefficient of the propeller is defined by its pitch setting, its advance ratio and the slopes of the thrust coefficient lines in the open water propeller diagram:

$$\delta K_T^* = a\delta J^* + p\delta \theta^* \tag{9}$$

which can be expanded into:

$$\delta K_T^* = -a\delta n^* + a\delta v_s^* + p\delta \theta^* - a\delta w^* \tag{10}$$

This equation can be implemented into the state-space system, resulting in δK_T^* as a system output. Note that Eq. (10) implies that changes in inflow, rotation speed and propeller pitch instantaneously result in changes in thrust coefficient. This is a common assumption which neglects the fast dynamics related to the change in circulation around the propeller blades. To investigate the effect of this common assumption, replacement of the static propeller model (based on the derivatives of the open water diagram) with a dynamic propeller model is recommended.

3.2. The cavitation number

The cavitation number σ_n is defined by:

$$\sigma_n = \frac{p - p_v}{1/2 \rho n^2 D^2} \tag{11}$$

in which p_v is the vapour pressure of water and p is the pressure at the shaft centre line without the influence of the propeller. The difference between the two is made dimensionless with the rotational speed of the propeller. Although the definition of cavitation number as used here is common, it has to be mentioned that other definitions do exist, see for example Carlton (2007). Because the vapour pressure can be taken as a constant, a normalised and linearised form of Eq. (11) is given by:

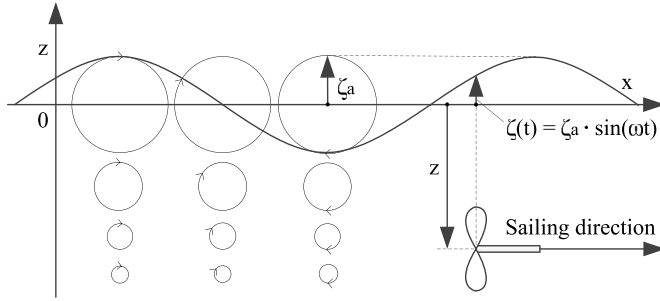$$\delta \sigma_n^* = \delta p^* - 2\delta n^* \tag{12}$$

Fig. 3. Sign convention and nomenclature.

As can be seen from Eq. (12), a linearised form of the pressure at the location of the shaft centerline has to be found. To find such an expression, we start with the linearised Bernoulli equation for unsteady flow:

$$p(t) = -\rho \frac{\partial \Phi}{\partial t} - \rho g z + p_a \tag{13}$$

The first term of Eq. (13) is the unsteady pressure fluctuation, the second term is the hydrostatic pressure and the last term is the atmospheric pressure. The unsteady pressure fluctuation at some shaft submergence z, under the influence of a harmonic *deep water* wave, is given by:

$$-\rho \frac{\partial \Phi}{\partial t} = \rho g e^{kz} \cdot \zeta(t) \tag{14}$$

In Eq. (14), the sea surface elevation is denoted by $\zeta(t)$ and is positive upwards and 0 at still water level, see Fig. 3. For deep water waves, the wavenumber k is given by:

$$k = \frac{\omega^2}{g} \tag{15}$$

Substituting Eq. (14) back into Eq. (13) yields:

$$p(t) = \rho g e^{kz} \cdot \zeta(t) - \rho g z + p_a \tag{16}$$

which can also be written as:

$$p_0 + \delta p = \rho g e^{k(z_0 + \delta z)} \cdot (\zeta_0 + \delta \zeta) - \rho g(z_0 + \delta z) + p_{a,0} + \delta p_a \tag{17}$$

According to the coordinate system of Fig. 3, ζ_0 is equal to 0 (the still water level does not change) so that $\zeta(t) = \delta \zeta$. Because ship motions are neglected in this analysis δz is also equal to 0. Furthermore, since variations in atmospheric pressure take place at a way larger timescale than wave encounters, $\delta p_a = 0$. With these simplifications, Eq. (17) reduces to Eq. (18).

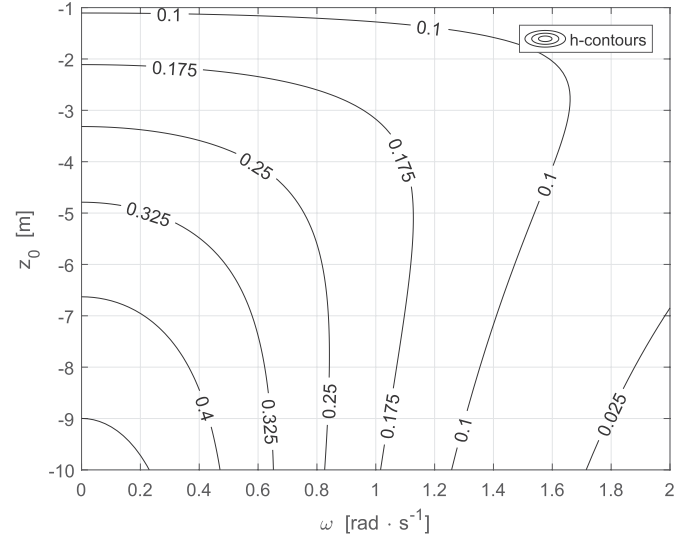$$p_0 + \delta p = \rho g e^{kz_0} \cdot \delta \zeta - \rho g z_0 + p_{a,0} \tag{18}$$

The equilibrium pressure is given by:

$$p_0 = -\rho g z_0 + p_{a,0} \tag{19}$$

Subtracting Eq. (19) from Eq. (18) yields:

$$\delta p = \rho g e^{kz_0} \cdot \delta \zeta \tag{20}$$

According to Eq. (20), the pressure variation is a linear function of the sea surface elevation $\delta \zeta$ at a given wave number k and still water shaft submergence z_0. Next, the pressure variation δp is normalised with the equilibrium pressure and the sea surface elevation is normalised with the negative of the (negative) still water shaft submergence z_0. In this way, a wave crest corresponds to a positive $\delta \zeta^*$. As a result:

Fig. 4. Contour plot of the pressure coefficient h.

$$\frac{\delta p}{p_0} = \frac{\rho g \cdot e^{kz_0}}{-\rho g z_0 + p_{a,0}} \cdot \frac{-z_0}{-z_0} \cdot \delta \zeta$$

$$\delta p^* = \frac{-\rho g z_0 \cdot e^{kz_0}}{-\rho g z_0 + p_{a,0}} \cdot \delta \zeta^* \tag{21}$$

or:

$$\delta p^* = h \delta \zeta^* \tag{22}$$

with:

$$h = \frac{-\rho g z_0 \cdot e^{kz_0}}{-\rho g z_0 + p_{a,0}} \tag{23}$$

$$\delta p^* = \frac{\delta p}{p_0} = \frac{\delta p}{-\rho g z_0 + p_{a,0}} \tag{24}$$

$$\delta \zeta^* = \frac{\delta \zeta}{-z_0} = \frac{\zeta(t)}{-z_0} \tag{25}$$

Substituting Eq. (22) back into Eq. (12) yields the final linearised and normalised expression for the cavitation number:

$$\delta \sigma_n^* = h \delta \zeta^* - 2 \delta n^* \tag{26}$$

The pressure coefficient h predominantly varies with still water shaft submergence z_0 and wave frequency ω (hidden in the wave number k). Due to the frequency dependency of h, analysis is limited to one frequency at a time. A contour plot of h is shown in Fig. 4. The shape of the contour lines can be understood by imagining what the individual contribution is of the 'hydrostatic' $\frac{-\rho g z_0}{-\rho g z_0 + p_{a,0}}$ and the 'exponential' e^{kz_0} term which make up h. Since the hydrostatic term is frequency independent, its value only varies along the vertical axis of Fig. 4. Because the contribution of the hydrostatic pressure to the total pressure obviously goes to 0 for zero shaft submergence, so does h, explaining the low value in the upper part of the domain. On the contrary, for infinite shaft submergence, the contribution of the atmospheric pressure is negligible so in that case, the hydrostatic term approaches 1. At the bottom of the domain of Fig. 4, the hydrostatic term is approximately 0.5. For either low wave frequency or low shaft submergence, the exponential term has a value near 1. As a result, the left and upper part of the domain are governed by the hydrostatic term.

However, for increasing wave frequency and or shaft submergence, the exponential term approaches 0. For that reason, the value of h decreases towards the lower right corner of the domain.

3.3. Wake disturbance as a function of sea surface elevation

An *undisturbed* axial wave velocity component is added to the propeller advance speed as a disturbance:

$$v_a = v_s(1 - w) - u_x \tag{27}$$

In principle, it is a choice to add or subtract u_x dependent on the definition of positive direction. Eq. (27) can also be written as:

$$v_{a,0} + \delta v_a = (v_{s,0} + \delta v_s) \cdot (1 - (w_0 + \delta w)) - (u_{x,0} + \delta u_x) \tag{28}$$

or:

$$v_{a,0} + \delta v_a = v_{s,0} - v_{s,0} \cdot w_0 - v_{s,0} \cdot \delta w + \delta v_s - \delta v_s \cdot w_0 - \delta v_s \cdot \delta w - u_{x,0} - \delta u_x \tag{29}$$

As there is no constant component in the undisturbed wave velocity, $u_{x,0} = 0$. Furthermore, the second order term is neglected. As a result, Eq. (29) reduces to:

$$v_{a,0} + \delta v_a = v_{s,0} - v_{s,0} \cdot w_0 - v_{s,0} \cdot \delta w + \delta v_s - \delta v_s \cdot w_0 - \delta u_x \tag{30}$$

The equilibrium advance speed is given by:

$$v_{a,0} = v_{s,0}(1 - w_0) = v_{s,0} - v_{s,0} \cdot w_0 \tag{31}$$

Subtracting Eq. (31) from Eq. (30) results in:

$$\delta v_a = -v_{s,0} \cdot \delta w + \delta v_s - \delta v_s \cdot w_0 - \delta u_x$$

$$\delta v_a = \delta v_s \cdot (1 - w_0) - v_{s,0} \cdot \delta w - \delta u_x \tag{32}$$

Division of both sides by the equilibrium advance speed of Eq. (31) yields normalised terms:

$$\frac{\delta v_a}{v_{a,0}} = \frac{\delta v_s}{v_{s,0}} - \frac{\delta w}{(1 - w_0)} - \frac{\delta u_x}{v_{a,0}} \tag{33}$$

or by the shorthand notation for differential increments:

$$\delta v_a^* = \delta v_s^* - \delta w^* - \delta u_x^* \tag{34}$$

The axial velocity of water particles in a 2-dimensional harmonic deep water wave at shaft centerline submergence z, is given by:

$$\delta u_x = \omega e^{kz} \cdot \zeta_a \sin(\omega t) \tag{35}$$

Note that the particle velocity is a function of the sea surface elevation ($\delta \zeta = \zeta_a \sin(\omega t)$). In other words, the axial particle velocity and pressure reach their maxima at the same time. However, unlike the pressure, obviously the particle velocity has a direction. Since this analysis is limited to axial wake velocities, we have to introduce $cos(\mu)$ in which μ is the ship heading relative to the waves. By sign convention, $\mu = 0°$ for following waves and $\mu = 180°$ for head waves. So we find:

$$\delta u_x = cos(\mu) \cdot \omega e^{kz} \cdot \delta \zeta \tag{36}$$

Because it is assumed that the wave disturbance velocity at shaft centerline submergence is equal over the entire propeller disk and ship motions are neglected, $e^{kz} = e^{kz_0}$. Furthermore, similar as in the previous subsection, the sea surface elevation $\delta \zeta$ is normalised with the negative of the shaft submergence $-z_0$. Moreover, according to Eq. (33), δu_x has to be normalised with the equilibrium advance speed $v_{a,0}$, which results in:

$$\frac{\delta u_x}{v_{a,0}} = \frac{cos(\mu) \cdot \omega e^{kz_0}}{v_{a,0}} \cdot \frac{-z_0}{-z_0} \cdot \delta \zeta$$
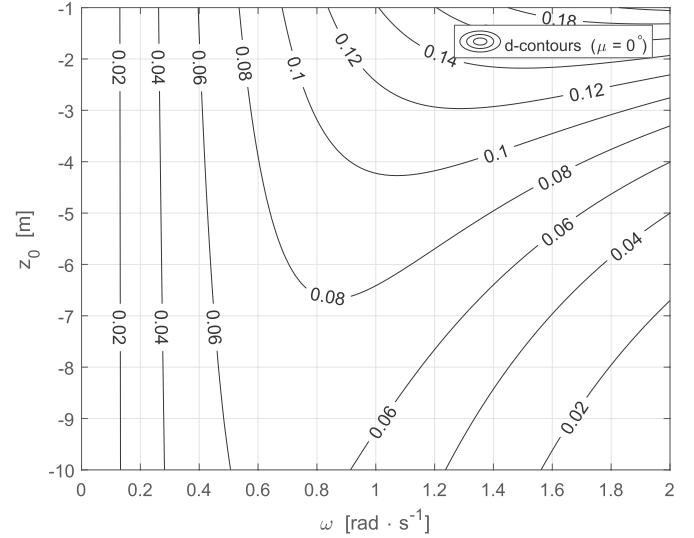

Fig. 5. Contour plot of the wake disturbance coefficient d.

$$\delta u_x^* = \frac{-z_0 \cdot cos(\mu) \cdot \omega e^{kz_0}}{v_{a,0}} \cdot \delta \zeta^* \tag{37}$$

From Eq. (34) it can be seen that in the normalised linear form, an axial wave velocity component has an equal effect on the propeller advance velocity as a disturbance in wake fraction. Because it is unnecessary to have multiple disturbance inputs for the propeller advance velocity, it is decided to just stick with the δw^* input only. This means that δu_x^* is removed from Eq. (34) and from now on δw^* equals δu_x^* from Eq. (37):

$$\delta w^* = \frac{-z_0 \cdot cos(\mu) \cdot \omega e^{kz_0}}{v_{a,0}} \cdot \delta \zeta^* \tag{38}$$

or:

$$\delta w^* = d \delta \zeta^* \tag{39}$$

with:

$$d = \frac{-z_0 \cdot cos(\mu) \cdot \omega e^{kz_0}}{v_{a,0}} \tag{40}$$

$$\delta w^* = \frac{\delta u_x}{v_{a,0}}$$

$$\delta \zeta^* = \frac{\delta \zeta}{-z_0} = \frac{\zeta(t)}{-z_0} \tag{41}$$

Eq. (40) shows that the wake disturbance coefficient d decreases linearly with increasing equilibrium advance speed. This aligns with intuition because the relative contribution of a disturbance velocity to
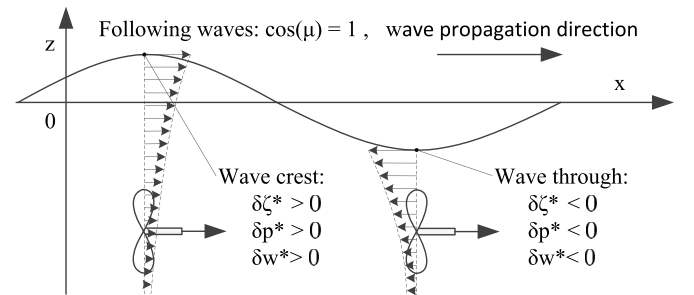

Fig. 6. Visualisation of the wake disturbance velocity for following waves.

Head waves: $\cos(\mu) = -1$, wave propagation direction

Wave crest:
$\delta\zeta^* > 0$
$\delta p^* > 0$
$\delta w^* < 0$

Wave through:
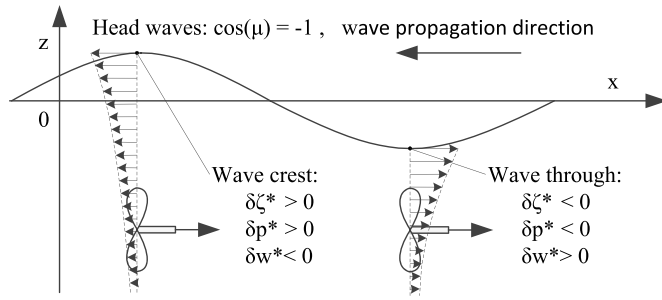$\delta\zeta^* < 0$
$\delta p^* < 0$
$\delta w^* > 0$

Fig. 7. Visualisation of the wake disturbance velocity for head waves.

the total advance velocity is low in case of a high equilibrium advance speed. For an equilibrium advance speed of 6.5 $m \cdot s^{-1}$, a contour plot of d is shown in Fig. 5.

Because the amplitude of the orbital wave velocity scales with ωe^{kz_0}, d approaches 0 for very low frequencies. However, for high frequencies and or shaft submergences, e^{kz_0} also goes to 0, explaining the low value of d in the bottom right corner of Fig. 5.

As a verification case for the sign conventions, consider a ship traveling in following waves, see Fig. 6. By definition, for following waves $\mu = 0$, so $\cos(\mu) = 1$. At the moment the propeller is located under a wave crest, $\delta\zeta^*$ is positive. Since the axial wave velocity is opposing the advance velocity, δw^* should be positive as well. According to Eq. (38), indeed this is the case (keep in mind that z_0 is always negative, so $-z_0$ is always positive). At the moment the propeller is located under a wave through when sailing in following seas, $\delta\zeta^*$ is negative and as a result δu_x^* is negative as well.

The wake disturbance velocities for head waves are visualised in Fig. 7, the verification is left for the reader.

3.4. Extended state-space model

A block diagram of the extended linear model is shown in Fig. 8. As can be seen, δp^* is added as an additional input to the core propulsion system. Moreover, as explained thoroughly in the previous subsections, the linearised and normalised pressure and wake fraction are written as a function of the sea surface elevation at encounter and included in the state-space model. In this way, $\delta\zeta^*$ conveniently is the only disturbance

input next to the ship resistance disturbance input $\delta\alpha^*$. However, the downside is that due to the frequency dependency of Eq. (22) and Eq. (39), state-space analysis is limited to one frequency at a time. An alternative to the chosen approach would be to generate the correlated disturbance signals δp^* and δw^* outside of the state-space model, allowing irregular wave (multi frequency) disturbance signals as time domain input.

The augmented state-space matrices of the extended uncontrolled system are given by:

$$A = \begin{bmatrix} \frac{(g+b-2)}{\tau_n} & \frac{-b}{\tau_n} & \frac{-q}{\tau_n} \\ \frac{(2-a)}{\tau_v} & \frac{(a-e)}{\tau_v} & \frac{p}{\tau_v} \\ 0 & 0 & \frac{-1}{\tau_\theta} \end{bmatrix}, \quad \mathbf{x} = \begin{bmatrix} \delta n^* \\ \delta v_s^* \\ \delta\theta^* \end{bmatrix}$$

$$B = \begin{bmatrix} \frac{v}{\tau_n} & 0 \\ 0 & 0 \\ 0 & \frac{1}{\tau_\theta} \end{bmatrix}, \quad \mathbf{u} = \begin{bmatrix} \delta X_{set}^* \\ \delta\theta_{set}^* \end{bmatrix}$$

$$G = \begin{bmatrix} 0 & \frac{d \cdot b}{\tau_n} \\ \frac{-1}{\tau_v} & \frac{-d \cdot a}{\tau_v} \\ 0 & 0 \end{bmatrix}, \quad \mathbf{w} = \begin{bmatrix} \delta\alpha^* \\ \delta\zeta^* \end{bmatrix}$$

$$\mathbf{y} = \begin{bmatrix} \delta n^* \\ \delta v_s^* \\ \delta\theta^* \\ \delta M_b^* \\ \delta K_T^* \\ \delta\sigma_n^* \end{bmatrix}, \quad C = \begin{bmatrix} 1 & 0 & 0 \\ 0 & 1 & 0 \\ 0 & 0 & 1 \\ g & 0 & 0 \\ -a & a & p \\ -2 & 0 & 0 \end{bmatrix}$$

$$D = \begin{bmatrix} 0 & 0 \\ 0 & 0 \\ 0 & 0 \\ v & 0 \\ 0 & 0 \\ 0 & 0 \end{bmatrix}, \quad H = \begin{bmatrix} 0 & 0 \\ 0 & 0 \\ 0 & 0 \\ 0 & 0 \\ 0 & -d \cdot a \\ 0 & h \end{bmatrix} \quad (42)$$

By applying the control law as given by Eqs. (6)–(8), the engine speed controlled system is obtained:
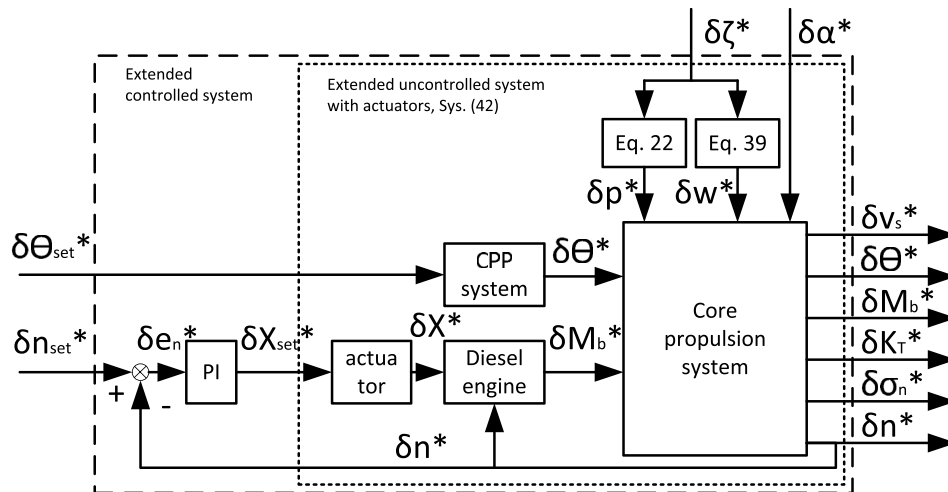

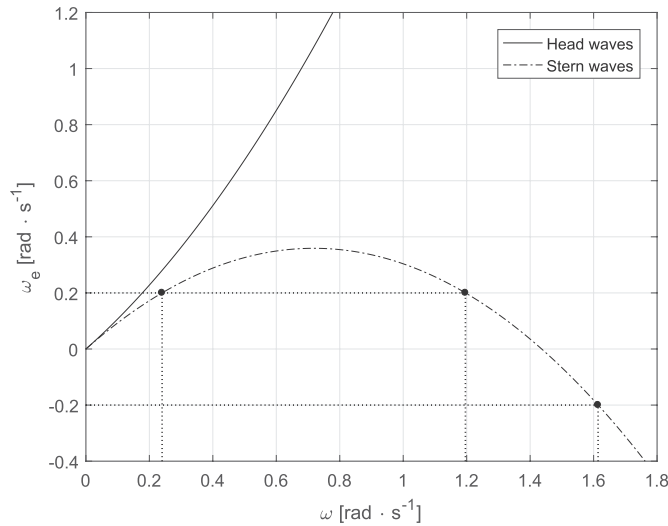**Fig. 8.** Schematic ship propulsion system, new extensions included.

Fig. 9. Wave encounter frequency ω_e as a function of wave frequency ω for $v_{s,0} = 6.83\,m\cdot s^{-1}$.

$$
A = \begin{bmatrix} \frac{(g+b-2-vK_p)}{\tau_n} & \frac{-b}{\tau_n} & \frac{-q}{\tau_n} & \frac{vK_i}{\tau_n} \\ \frac{(2-a)}{\tau_v} & \frac{(a-e)}{\tau_v} & \frac{p}{\tau_v} & 0 \\ 0 & 0 & \frac{-1}{\tau_\theta} & 0 \\ -1 & 0 & 0 & 0 \end{bmatrix} \mathbf{x} = \begin{bmatrix} \delta n^* \\ \delta v_s^* \\ \delta \theta^* \\ \delta E_n^* \end{bmatrix},
$$

$$
B = \begin{bmatrix} \frac{vK_p}{\tau_n} & 0 \\ 0 & 0 \\ 0 & \frac{1}{\tau_\theta} \\ 1 & 0 \end{bmatrix},\quad \mathbf{u} = \begin{bmatrix} \delta n_{set}^* \\ \delta \theta_{set}^* \end{bmatrix}
$$

$$
G = \begin{bmatrix} 0 & \frac{d\cdot b}{\tau_n} \\ \frac{-1}{\tau_v} & \frac{-d\cdot a}{\tau_v} \\ 0 & 0 \\ 0 & 0 \end{bmatrix},\quad \mathbf{w} = \begin{bmatrix} \delta \alpha^* \\ \delta \zeta^* \end{bmatrix}
$$

$$
\mathbf{y} = \begin{bmatrix} \delta n^* \\ \delta v_s^* \\ \delta \theta^* \\ \delta E_n^* \\ \delta M_b^* \\ \delta K_T^* \\ \delta \sigma_n^* \end{bmatrix},\quad C = \begin{bmatrix} 1 & 0 & 0 & 0 \\ 0 & 1 & 0 & 0 \\ 0 & 0 & 1 & 0 \\ 0 & 0 & 0 & 1 \\ g-vKp & 0 & 0 & vK_i \\ -a & a & p & 0 \\ -2 & 0 & 0 & 0 \end{bmatrix}
$$

$$
D = \begin{bmatrix} 0 & 0 \\ 0 & 0 \\ 0 & 0 \\ 0 & 0 \\ vK_p & 0 \\ 0 & 0 \\ 0 & 0 \end{bmatrix},\quad H = \begin{bmatrix} 0 & 0 \\ 0 & 0 \\ 0 & 0 \\ 0 & 0 \\ 0 & 0 \\ 0 & -d\cdot a \\ 0 & h \end{bmatrix}
$$

$$\tag{43}$$

4. Disturbance input and simulations

As evident from the previous subsections, the sea surface elevation at the location of the propeller is required as minimum disturbance input in order to analyse the behaviour of the propeller operating point in the cavitation diagram. In this section, it is explained briefly how the $\delta\zeta^*$ disturbance is generated. Subsequently, the behaviour of the engine speed controlled system is studied based on the corresponding Bode plots and operating ellipses in the cavitation bucket and engine

envelope.

4.1. Sea surface elevation at encounter

First, recall that in deriving δp^* and δw^*, it was assumed that the sea surface elevation at the location of the propeller is the result of a single, harmonic, deep water wave component. Also, all hull influences were neglected, i.e. the incoming wave is undisturbed, and radiated plus diffracted wave components are neglected.

Due to the speed of the vessel, the wave encounter frequency ω_e differs from the wave frequency and is given by:

$$\omega_e = \omega - \frac{\omega^2}{g}\cdot v_s\cdot cos(\mu) \tag{44}$$

or:

$$\omega_e = \omega - k\cdot v_s\cdot cos(\mu) \tag{45}$$

In calculating the wave encounter frequency, variations in ship speed are neglected so v_s is replaced by $v_{s,0}$:

$$\omega_e = \omega - k\cdot v_{s,0}\cdot cos(\mu) \tag{46}$$

Subsequently, the sea surface elevation at encounter can simply be calculated by:

$$\delta\zeta = \zeta_a\cdot sin(\omega_e t) \tag{47}$$

After normalisation of $\delta\zeta$ with $-z_0$ (see Eq. (25)), the normalised sea surface elevation $\delta\zeta^*$ is obtained:

$$\delta\zeta^* = \frac{\zeta_a}{-z_0}\cdot sin(\omega_e t) \tag{48}$$

To get a feeling for the range of possible wave encounter frequencies, Eq. (46) is evaluated for an equilibrium ship advance speed of $v_{s,0} = 6.83\ m\cdot s^{-1}$, the results are shown in Fig. 9.

As can be seen from Fig. 9, when sailing in head waves ($\mu = 180°$), the wave encounter frequency rapidly increases with wave frequency. As a result, the wave *encounter* frequency is uniquely related to the *wave* frequency for head waves. However, when sailing in stern waves, Fig. 9 shows that in some cases three different wave frequencies could result in the same wave encounter frequency. In other words, the wave encounter frequency is *not* uniquely related to the *wave* frequency in case of stern waves. The dots in Fig. 9 are an example of this phenomenon. Also note, that in this case, waves having a frequency lower than approximately 1.44 $rad\cdot s^{-1}$ travel faster than the ship and waves having a higher frequency propagate slower than the ship.

4.2. Bode plots of the engine speed controlled system

In the previous subsection it is shown that multiple wave frequencies can result in the same wave encounter frequency. Since the extended state-space system (Sys. (42)) is wave frequency dependent, the system response for a certain wave encounter frequency is in most cases non unique when sailing in stern waves. Due to that, it is not straightforward to construct Bode plots corresponding to stern waves. For that reason, it is decided to construct Bode plots corresponding to head waves only. Moreover, due to the frequency dependency of h and d, Bode plots need to be generated by looping through all frequencies individually.

The Bode plots of the extended uncontrolled system and of the extended controlled system, showing the frequency response of $\delta\sigma_n^*$, δK_T^*, δM_b^* and δn^* to a $\delta\zeta^*$ disturbance input are shown in Fig. 10a, b, 10c and 10d respectively. It is decided to only show the frequency response of these variables because they define the behaviour of the operating point in a cavitation inception diagram and engine envelope and are therefore *directly* related to cavitation inception and engine loading.
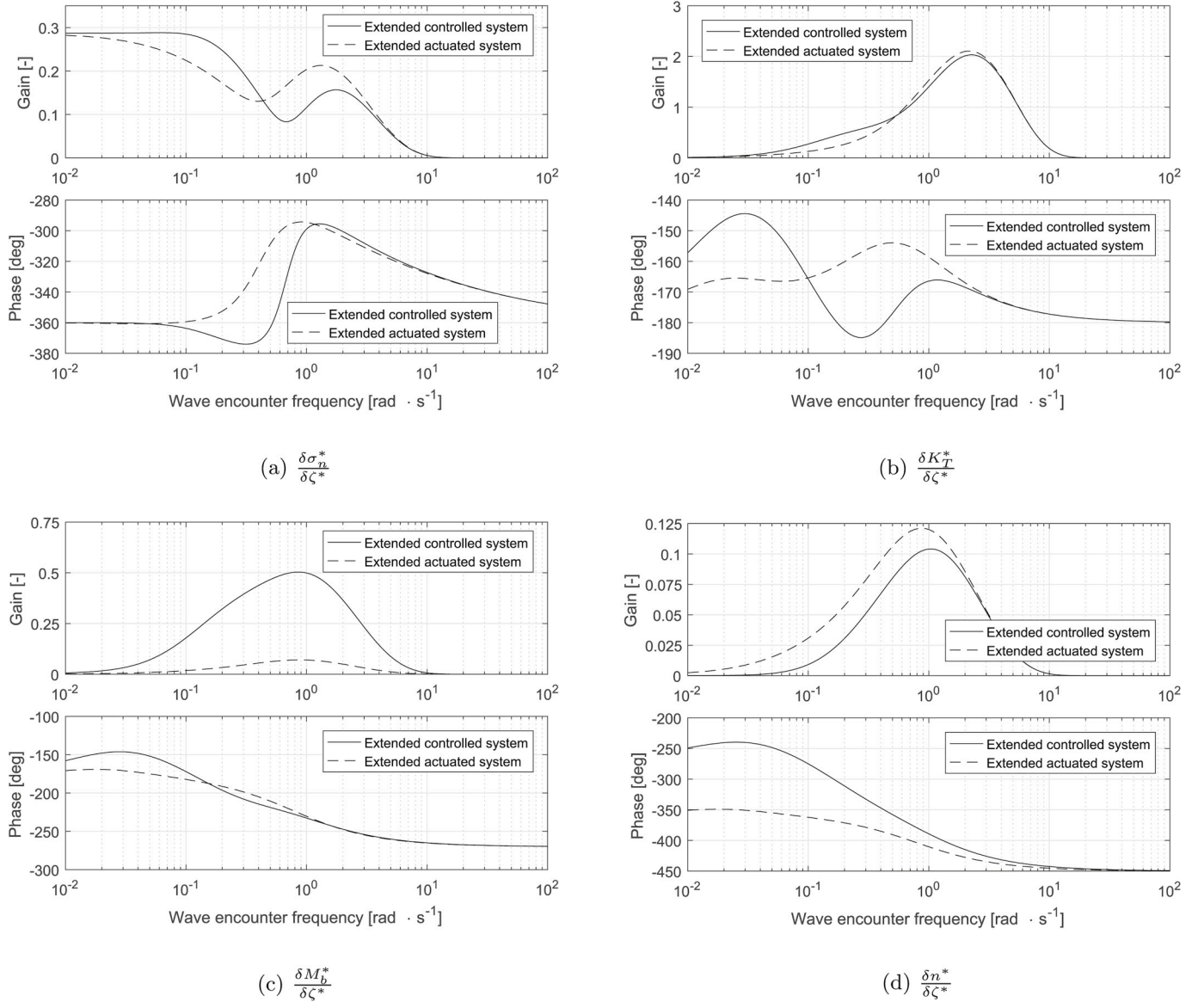
(a) $\frac{\delta\sigma_n^*}{\delta\zeta^*}$

(b) $\frac{\delta K_T^*}{\delta\zeta^*}$

(c) $\frac{\delta M_b^*}{\delta\zeta^*}$

(d) $\frac{\delta n^*}{\delta\zeta^*}$

Fig. 10. Bode plots related to sea surface elevation, actuated system and engine speed controlled system, $\mu = 180°$, $K_p = 2$, $K_i = 1$.

Table 1
Parameters and variables at the equilibrium operating point.

| a	normalised prop derivative	-5.404	[-]
b	norm. propeller derivative	-3.499	[-]
p	norm. propeller derivative	6.580	[-]
q	norm. propeller derivative	5.025	[-]
e	norm. resistance derivative	1.861	[-]
g	norm. engine derivative	-0.582	[-]
v	norm. engine derivative	1.910	[-]
$K_{T,0}$	nominal propeller thrust coefficient	0.115	[-]
$K_{Q,0}$	nominal propeller torque coefficient	0.0245	[-]
J_0	nominal advance ratio	0.93	[-]
τ_n	shaft speed integration constant	7.835	[s]
τ_v	ship speed integration constant	115.692	[s]
τ_θ	propeller pitch time constant	2	[s]
ρ	seawater density	1025	[$kg \cdot m^{-3}$]
g	gravitational acceleration	9.81	[$m \cdot s^{-2}$]
z_0	nominal propeller submergence	-4	[m]
$p_{a,0}$	nominal ambient air pressure	10^5	[Pa]
$v_{a,0}$	nominal speed of advance	6.489	[$m \cdot s^{-1}$]

Fig. 10a shows that the $\delta\sigma_n^*$ response is rather frequency independent at the lowest wave encounter frequencies. The gain in this region is the sole result of the pressure difference δp^* caused by the variation in shaft submergence. The variations in δp^* decrease with increasing encounter (and thus wave) frequency (see Fig. 4 for the h contours). However, the engine speed response δn^* causes a small local peak in $\delta\sigma_n^*$ response at a wave encounter frequency of around 1.5 $rad \cdot s^{-1}$. For frequencies exceeding 10 $rad \cdot s^{-1}$, both variations in engine speed and pressure are negligible.

Fig. 10b shows that at low wave encounter frequencies, there is almost no effect of sea surface elevation (and thus δw^*) on propeller thrust coefficient. This is because at these low frequencies, a change in propeller advance velocity results in a change of propeller thrust which results in a change of ship speed which has a restoring effect on the advance ratio and thus on K_T.

At a relatively high encounter frequency of 2.5 $rad \cdot s^{-1}$ there is a peak in thrust coefficient gain. As can be seen, the peak in gain of the extended controlled and extended actuated system is about the same. At even higher encounter frequencies, the d coefficient goes to 0 (see Fig. 5) resulting in 0 wake disturbance and hence 0 δK_T^*.
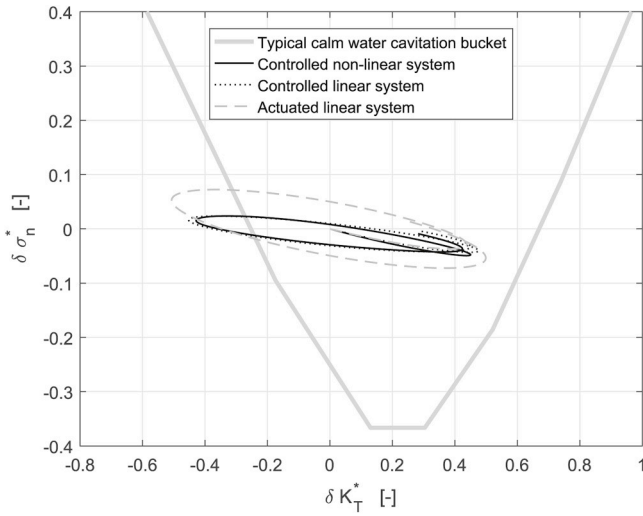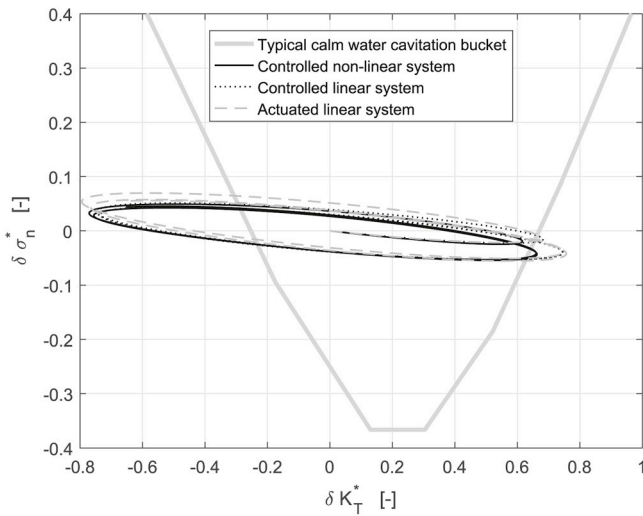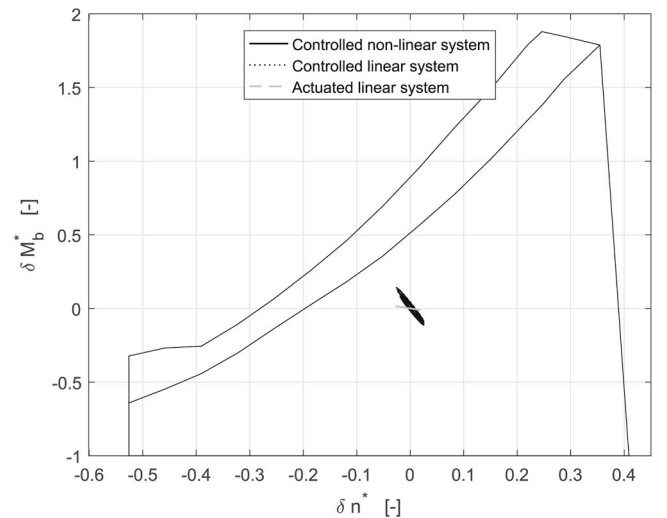
(a) Cavitation bucket
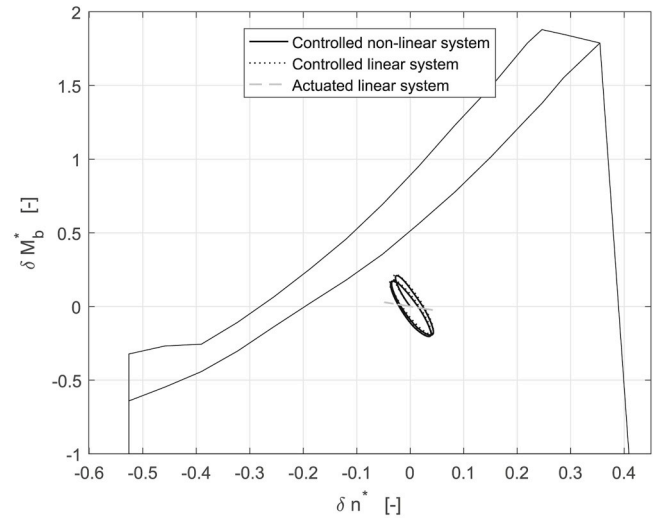
(b) Engine envelope

Fig. 11. Operating ellipses for head waves ($\mu = 180°$), $\zeta_a = 1.5m$, $\omega = 0.6 \; rad·s^{-1}$ $\omega_e = 0.851 \; rad·s^{-1}$.

(a) Cavitation bucket

(b) Engine envelope

Fig. 12. Operating ellipses for head waves ($\mu = 180°$), $\zeta_a = 1.5m$, $\omega = 1.4 \; rad·s^{-1}.\omega_e = 2.765 \; rad·s^{-1}$.

From Fig. 10d it can be observed that indeed, the governor reduces the variations in engine speed over a wide range of frequencies. However, this comes at the cost of considerable brake torque variations to be delivered by the diesel engine, see Fig. 10c.

The frequency domain behaviour as presented here will change for different operating points and or different controller structures and parameter settings. The variables and parameters of the operating point under consideration are given in Table 1. Other nominal values of system variables in the selected operating point are listed in Stapersma and Vrijdag (2017) and Vrijdag and Stapersma (2017).
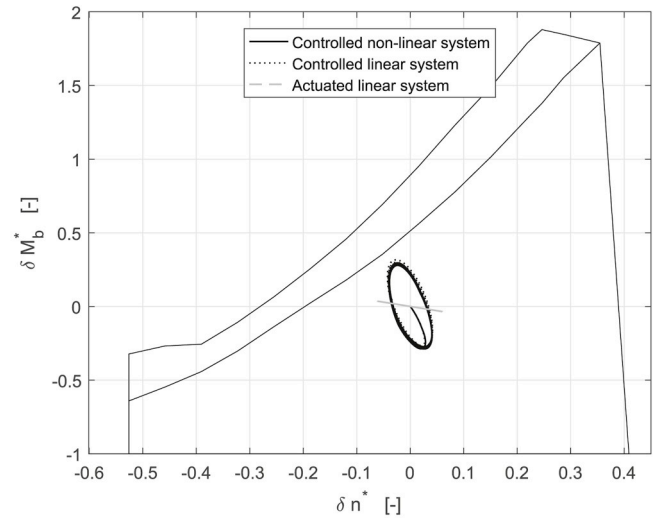
4.3. Operating ellipses

Based on the previously discussed Bode plots, the operating ellipses in both the engine envelope and cavitation bucket corresponding to wave frequencies of 0.6 and 1.4 $rad·s^{-1}$ are shown in Figs. 11 and 12 for head waves and in Figs. 13 and 14 for stern waves. Note that the effect of seaway on ship resistance is not included, which makes that the centre of the ellipses in all cases lie at the same location, which is not true in reality. This does however allow us to focus on the size of the

wave induced effect on pressure and propeller wakefield and therefore on the size of the ellipses. Further note that besides the operating ellipses corresponding to the extended actuated linear system and the extended engine speed controlled linear system, also non-linear results for the engine speed controlled system are plotted for verification reasons.

Even though it is assumed that the reader is familiar with the concept of a propeller cavitation inception diagram, the basics are explained briefly. First of all, it should be clear that when the operating point lies *inside* the cavitation 'bucket', the propeller operates free of cavitation. Conversely, if the operating point lies outside the bucket, the propeller suffers from *at least* one form of cavitation which results in an increased acoustic signature. The exact shape of the bucket depends on the propeller geometry and on the propeller wake field velocity *distribution*. When sailing in waves, the wake field velocity distribution continuously changes and so does the cavitation bucket. Therefore, the cavitation bucket is definitely not a fixed line when sailing in waves but should be seen as a dynamic boundary. It is therefore preferred to have the operating ellipse located inside the 'calm water' cavitation bucket with the margins as high as possible, reducing the likelihood of
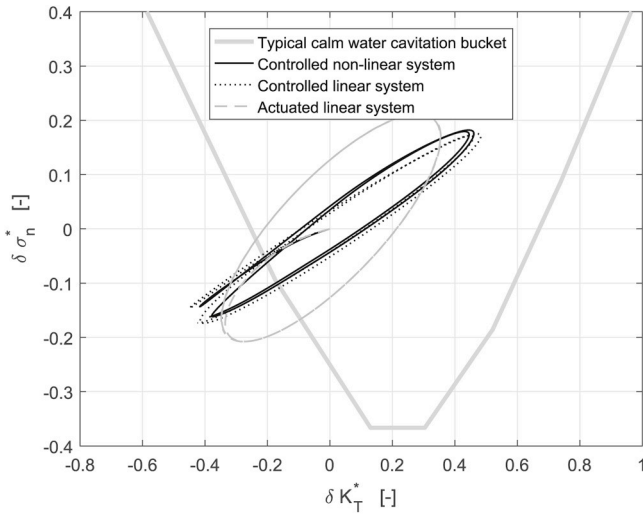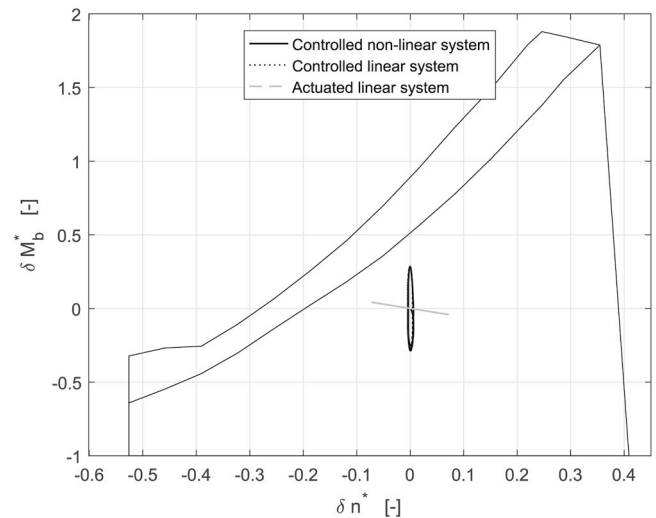
(a) Cavitation bucket

(b) Engine envelope

Fig. 13. Operating ellipses for stern waves ($\mu = 0°$), $\zeta_a = 1.5m$, $\omega = 0.6\ rad\cdot s^{-1}.\omega_e = 0.349\ rad\cdot s^{-1}$
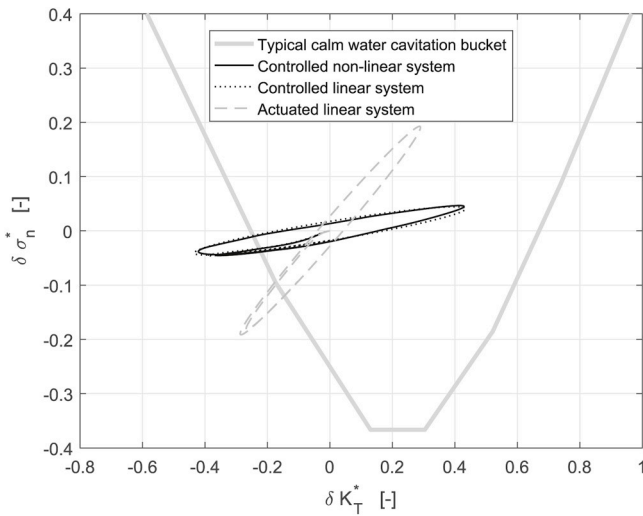
(a) Cavitation bucket

(b) Engine envelope

Fig. 14. Operating ellipses for stern waves ($\mu = 0°$), $\zeta_a = 1.5m$, $\omega = 1.4\ rad\cdot s^{-1}.\omega_e = 0.035\ rad\cdot s^{-1}$

Table 2
Governor gain settings.

K_p	K_i	
2	1	*as already used previously*
1	0	
1	2	
4	0	
4	2	

cavitation to occur.

From Figs. 11 and 12, three noteworthy observations are made. At first, note that the linear and non-linear model show good agreement, giving confidence that the linearised system is valid over a significant operating range. Secondly, note that at these particular encounter frequencies, the differences between the actuated and controlled system's operating ellipses in the cavitation bucket are relatively small. The small differences that are visible are fully explained by Fig. 10a and b. At last, note that the variations in thrust coefficient do increase significantly with wave encounter frequency as opposed to the variations

in brake torque and engine speed.

In contradiction to the head wave cases considered, Figs. 13 and 14 show that when sailing in stern waves, there is a noticeable difference in the cavitation bucket operating ellipse corresponding to the extended actuated- and extended controlled system. Apparently, for the ship and operating point under consideration, the low wave encounter frequency inherent to sailing in stern waves, allows the engine speed governor to have a considerable effect on both the size and orientation of the propeller operating ellipse in the cavitation bucket. This suggests that by either changing the controller gain settings, or controller structure, a more favorable operating ellipse in the inception diagram could be obtained, possibly reducing the amount of cavitation 'events' that occur when sailing in a seaway.

5. Effect of engine speed governor gain settings

In this section, it is shown how the governor gain settings affect the size and orientation of the cavitation bucket operating ellipse, possibly improving its positioning relative to the cavitation bucket. The engine speed control law of Eq. (6) is retained but the proportional and integral
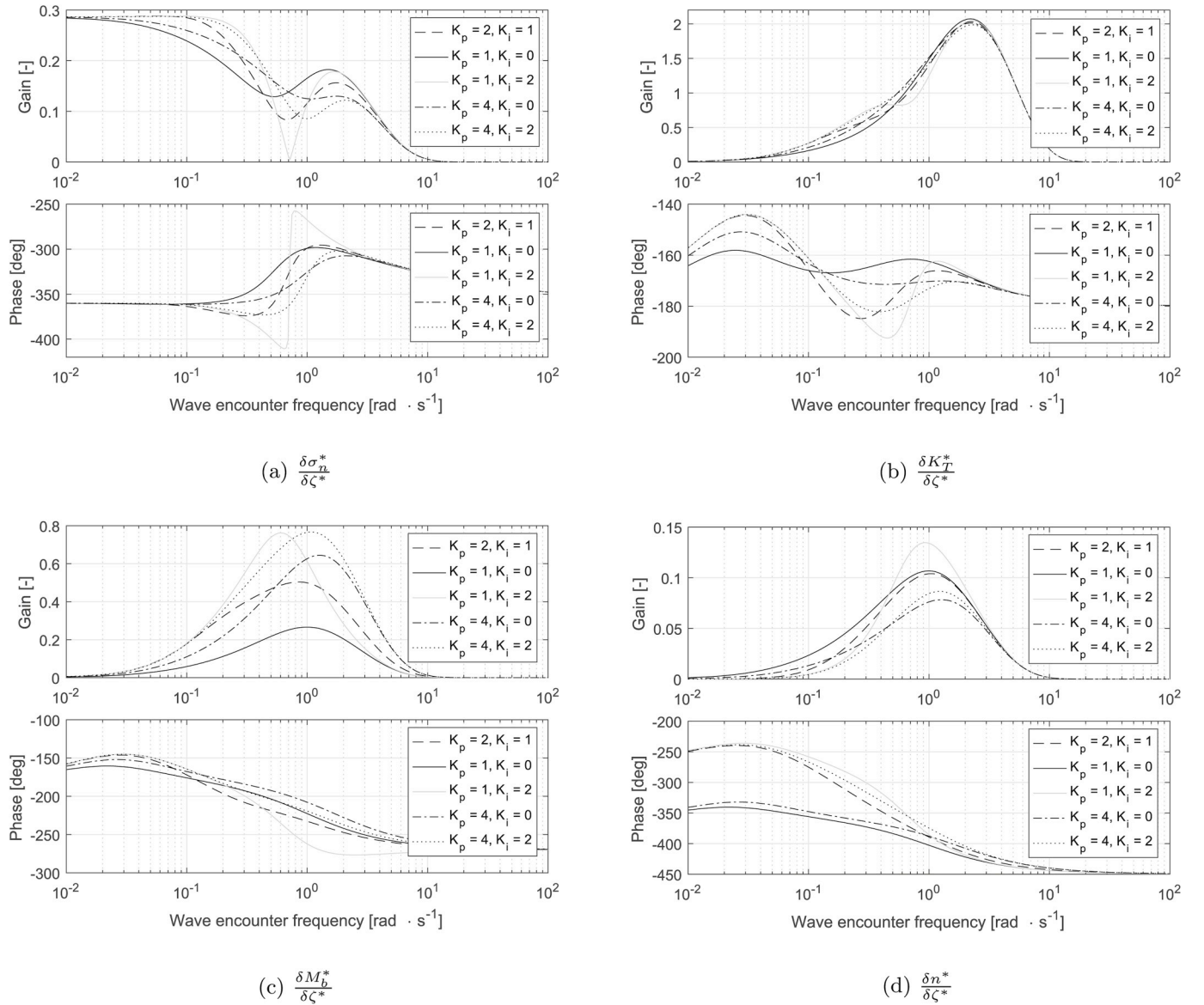
(a) $\frac{\delta\sigma_n^*}{\delta\zeta^*}$

(b) $\frac{\delta K_T^*}{\delta\zeta^*}$

(c) $\frac{\delta M_b^*}{\delta\zeta^*}$

(d) $\frac{\delta n^*}{\delta\zeta^*}$

Fig. 15. Bode plots related to sea surface elevation, engine speed controlled system $\mu = 180°$.

gains, K_p and K_i, are varied systematically. In addition to the gain settings used in the previous section ($K_p = 2$, $K_i = 1$), four combinations are chosen which surround the previously used settings in the K_p, K_i plane.

The chosen combinations are listed in Table 2. In a similar way as in the previous section, the Bode plots showing the $\delta\sigma_n^*$, δK_T^*, δM_b^* and δn^* frequency response to a $\delta\zeta^*$ disturbance input are shown in Fig. 15a, b, 15c and 15d respectively for head waves. The frequency responses corresponding to the gain combinations of Table 2 are plotted in the same graphs for easy comparison.

Fig. 15a shows that the combination of engine speed governor gains resulting in the lowest variations in cavitation number differs with wave encounter frequency. In other words, there does not seem to be a single combination of governor gains which, from cavitation number variations perspective, is most favorable. Nevertheless, by comparing Fig. 15a and b (along with the results of the previous section) it should be concluded that it is more important to reduce the variations in thrust coefficient than variations in cavitation number. This is, because over the larger part of the domain the thrust coefficient gain is significantly

higher than the cavitation number gain. However, as can be seen from Fig. 15b, for the lower range of wave encounter frequencies, the differences in thrust coefficient variations between different gain combinations are small. For the higher range of wave encounter frequencies the difference is negligible, which does not look very promising.

From Figs. 15c and d it can be observed that governor gain combinations with high integral gain seem to invoke high variations in torque while not significantly reducing the variations in engine speed compared to gain combinations with a lower or 0 integral gain. Based on this, it seems unnecessary to apply a large integral gain.

The discussed frequency response amplitudes are highly valuable as they determine the size of the box which encloses an operating ellipse. However, they do not yet provide all information as the orientation, or shape of the operating ellipse within the box is governed by the difference in phase angle of the response of the two parameters under consideration. Because this phase difference is difficult to interpret from Bode plots, operating ellipses are constructed too, and discussed in the next subsection.
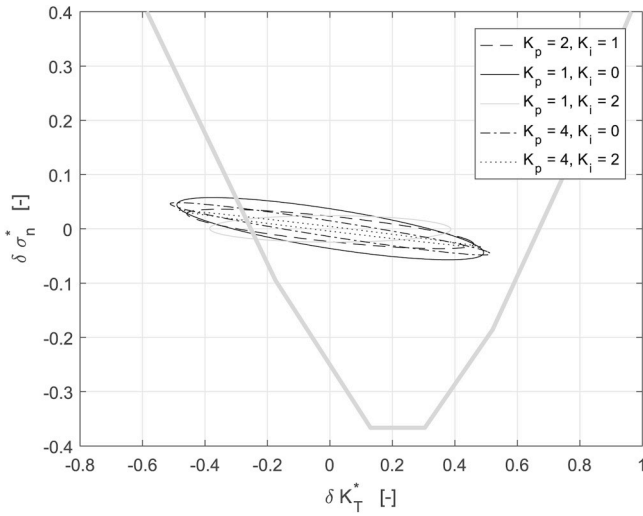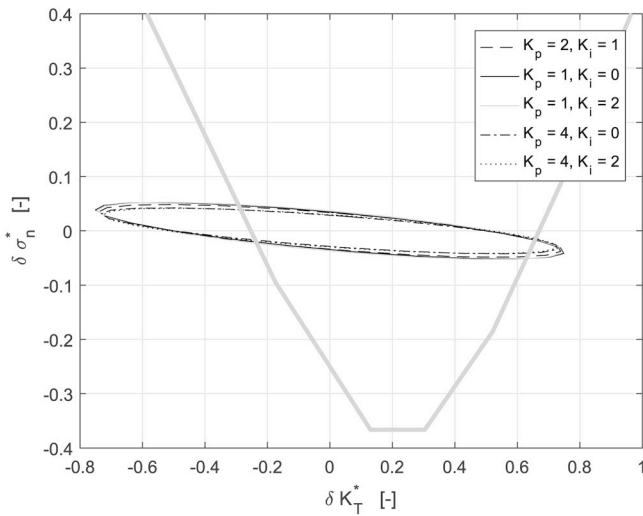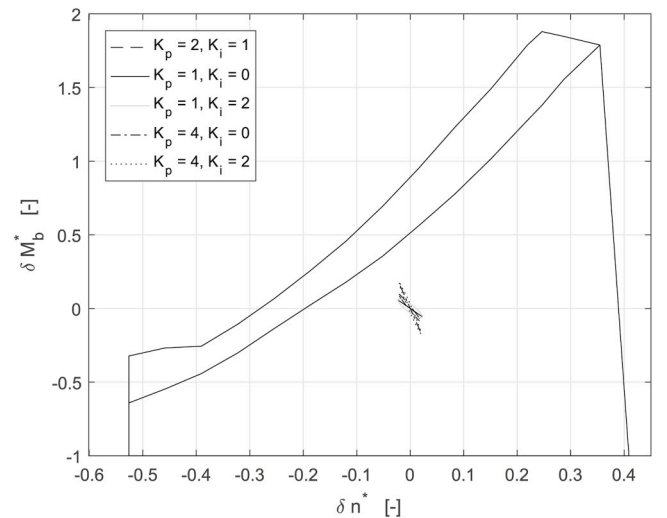
(a) Cavitation bucket
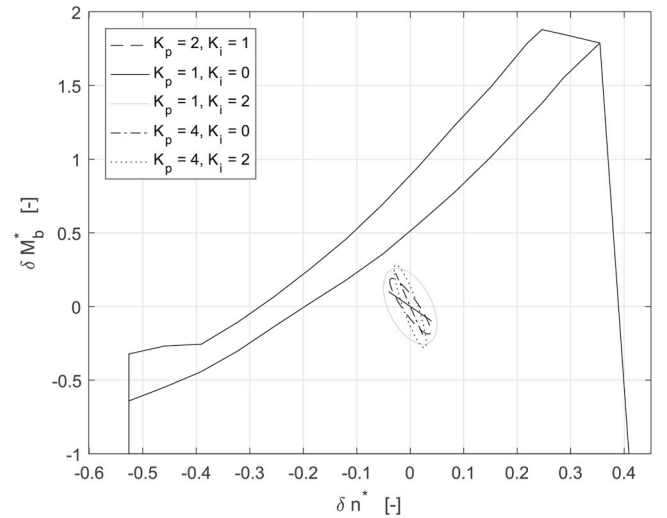
(b) Engine envelope

Fig. 16. Operating ellipses for head waves ($\mu = 180°$), $\zeta_a = 1.5m$, $\omega = 0.6\ rad·s^{-1}$ $\omega_e = 0.851\ rad·s^{-1}$.

(a) Cavitation bucket

(b) Engine envelope

Fig. 17. Operating ellipses for head waves ($\mu = 180°$), $\zeta_a = 1.5m$, $\omega = 1.4\ rad·s^{-1}$ $\omega_e = 2.765\ rad·s^{-1}$.

5.1. Operating ellipses

The operating ellipses corresponding to the engine speed governor gain settings listed in Table 2 are shown in Figs. 16 and 17 for head waves and in Figs. 18 and 19 for stern waves. The ellipses correspond to a wave amplitude of $1.5\ m$ and wave frequencies of 0.6 and $1.4\ rad·s^{-1}$ respectively (similar conditions as in Section 4.3).

When looking at Fig. 16, note that the operating ellipse corresponding to the governor gain combination $K_p = 1$, $K_i = 2$ is the smallest ellipse in the cavitation bucket, but is also oriented slightly more horizontal compared to the other ellipses. On the contrary, the operating ellipse in the engine envelope corresponding to the same governor gain settings seems to be the largest of all ellipses.

From Fig. 17 it can be seen that at a wave encounter frequency of $2.765\ rad·s^{-1}$, the differences between the cavitation bucket operating ellipses is negligible, both with respect to size and orientation.

Regarding the engine envelope, it can be noted that the gain settings with the highest proportional gain show the largest variations in brake torque. Once again however, the increased variations in brake torque do not significantly reduce the variations in engine speed. All these

observations are in perfect agreement with the Bode plots of Fig. 15.

From Fig. 18 it can be observed that for stern waves, the cavitation bucket operating ellipses differ in orientation, but also slightly in size. Although the differences are small, in this case the operating ellipse corresponding to the governor gain combination $K_p = 1$, $K_i = 0$ seems to be favorable from cavitation perspective, but also in view of staying away from thermal engine limits. By coincidence, the governor gain combination $K_p = 1$, $K_i = 2$ is in this case least favorable, both from cavitation (in contradiction to Fig. 16a) as well as thermal engine loading perspective.

Fig. 19 shows, that for a wave frequency of $1.4\ rad·s^{-1}$, there are three governor gain combinations of which the operating ellipses virtually lie on top of each other, both in the cavitation bucket as well as in the engine envelope. Because for these governor gain combinations the variations in engine speed are small, the tilt in their cavitation bucket operating ellipses must be caused solely by the wave induced pressure variations. Furthermore, note that in this case, there is not really a clear best or worst combination of settings.
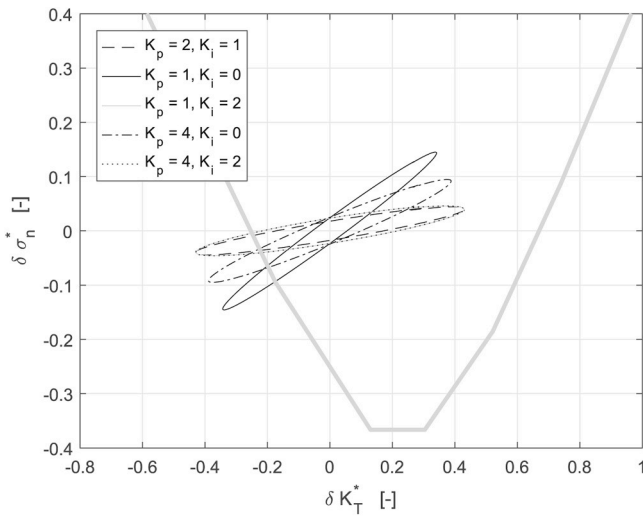
Both the Bode plots as well as the operating ellipses have revealed that the 'optimum' engine speed governor gain settings vary with wave
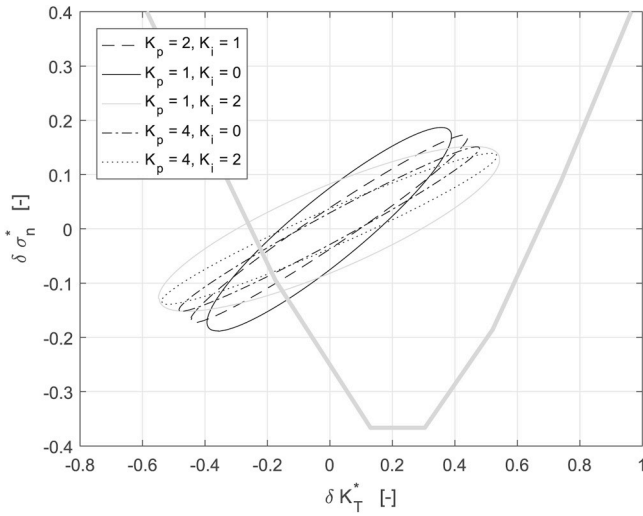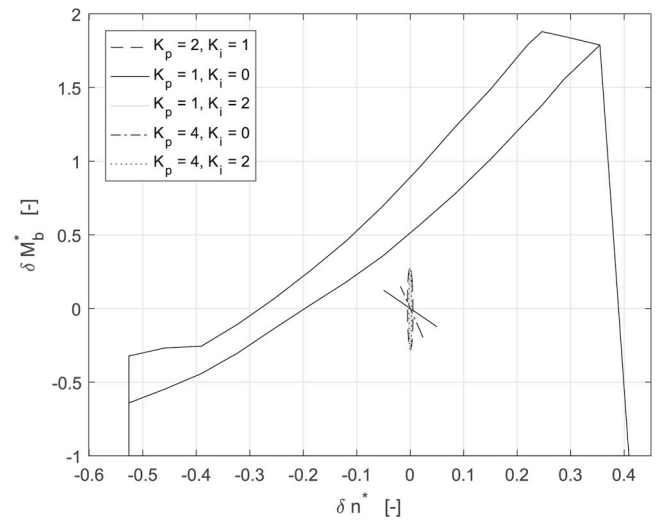
(a) Cavitation bucket
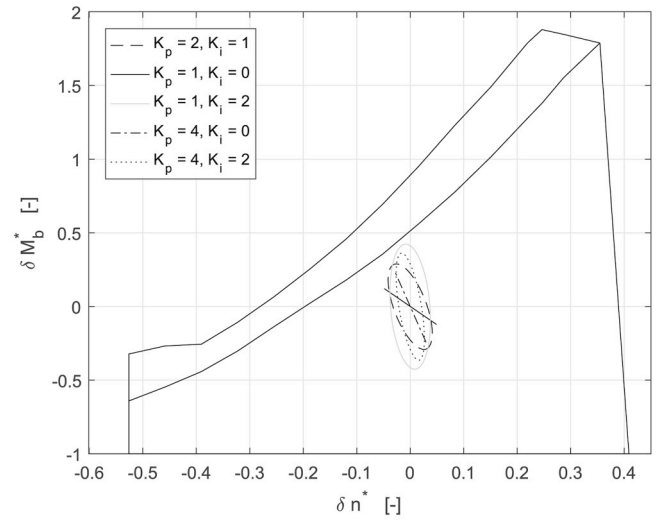
(b) Engine envelope

Fig. 18. Operating ellipses for stern waves ($\mu = 0°$), $\zeta_a = 1.5m$, $\omega = 0.6\ rad \cdot s^{-1}$. $\omega_e = 0.349\ rad \cdot s^{-1}$

(a) Cavitation bucket

(b) Engine envelope

Fig. 19. Operating ellipses for stern waves ($\mu = 0°$), $\zeta_a = 1.5m$, $\omega = 1.4\ rad \cdot s^{-1}$. $\omega_e = 0.035\ rad \cdot s^{-1}$

encounter frequency. On top of that, settings that could be favorable from cavitation viewpoint could, do not necessarily have to be favorable from engine thermal loading viewpoint and vice versa. This means that the system designer or user might have to prioritise between the two.

For the given ship and operating point, it looks impossible to *significantly* reduce the variations in thrust coefficient simply by applying different engine speed governor gain settings. The effect of these settings on cavitation inception in a seaway is therefore small. Nevertheless, the provided tools should enable researchers or engineers to develop, asses and tune the performance of alternative control strategies with respect to cavitation in a seaway.

6. Conclusions and recommendations

In this paper the linearised model that allows for the analysis of the behaviour of the engine operating point in the engine operating envelope and the propeller operating point in the cavitation diagram is derived and verified. The behaviour of the operating point in the diesel engine envelope is an indicator for thermal overloading of the diesel

engine, while the behaviour of the propeller operating point in the cavitation inception diagram should be seen as an indicator for cavitation and therefore for underwater radiated noise. Although not all intricacies of diesel engine overloading and cavitation inception in a seaway are included in the mentioned diagrams, they are useful for controller development and tuning.

The model was used to show how different wave encounter frequencies affect the system behaviour differently. Furthermore the difference in behaviour between a conventional engine speed controlled system and a non-controlled (fixed fuelrack) system was demonstrated.

The effect of changing engine speed governor gain settings on the behaviour in the engine envelope and in the cavitation bucket is explored. This leads to the conclusion that, for the selected ship and operating point, the potential for improvement of the shaft speed control law with respect to cavitation inception in a seaway is low because the variations in thrust coefficient can barely be reduced. Nonetheless, with this model it is now possible to use a rational approach to develop and tune alternative propulsion controllers, aiming to increase cavitation free time in a seaway while simultaneously preventing thermal overloading of the diesel engines. Alternative control strategies could for

instance make use of continuous propeller pitch variations to reduce variations in trust coefficient i.e. maintain acceptable angles of attack on the blade sections.

Although the model is successfully verified against a non-linear model, there are a number of limitations of the model. It is for instance not suited for the analysis of transients such as ship accelerations and decelerations. In such cases the non-linear behaviour of the propulsion plant and the (rate)-limiters included in its controllers, have a dominant effect on the system behaviour.

Furthermore, in its current form the model is not suited for irregular wave disturbances. If desired, it is recommended to generate the correlated δp^* and δw^* disturbance signals outside the state-space model by superposition with for example a random phase amplitude model.

There are many possible extensions and modifications that can be made to the model in order to make it approach reality closer. Various suggestions in that direction have been given in Stapersma and Vrijdag (2017) and Vrijdag and Stapersma (2017), the improvement of the CPP model for instance is one of them.

It is stressed that the linearised model does not replace a non-linear simulation model, but should be seen as an additional tool for propulsion controller development and tuning. In order to serve that purpose, it is concluded that it is important to keep it as simple as possible but as complex as necessary to capture the important dynamics for the problem under consideration.

References

Aalbers, A.B., van Gent, W., 1984. Unsteady wake velocities due to waves and motions measured on a ship model in head waves. In: Proc. of the 15th Symposium on Naval Hydrodynamics. Hamburg, pp. 69–81.

Bakker, J., Grimmelius, H.T., Wesselink, A., March, 2006. The use of non linear models in the analysis of cpp actuator behaviour. In: Proc. of the 2nd World Marit. Technology Conference (WMTC). IMarEST, London, isbn 1-902536-54-1.

Carlton, J.S., 2007. Marine Propellers and Propulsion. Buttersworth-Heineman Ltd ISBN 978-07506-8150-6.

Godjevac, M., 2009. Wear and Friction in a Controllable Pitch Propeller. Ph.D. thesis. Delft University of Technology ISBN 978-90-8891-136-1.

Jessup, S.D., Wang, H.-C., 1996. Propeller cavitation prediction for a ship in a seaway. In: Tech. rep., Carderock Division, Naval Surface Warfare Center, United States Navy.

Kuiper, G., Grimm, M., McNeice, B., Noble, D., Krikke, M., 2002. Propeller inflow at full scale during a manoeuvre. In: Proceedings of the 24th Symposium on Naval Hydrodynamics. Fukuoka, Japan. July 8–13.

Kuiper, G., Jessup, S.D., 1993. A propeller design method for unsteady conditions. SNAME transactions 101, 247–273.

Martelli, M., Figari, M., Altosole, M., Vignolo, S., 2014. Controllable pitch propeller actuating mechanism, modelling and simulation. Proc. Inst. Mech. Eng., Part M: J. of Eng. for the Marit. Environ. 228 (1). https://doi.org/10.1177/1475090212468254.

Rolland, R.M., Parks, S.E., Hunt, K.E., Castellote, M., Corkeron, P.J., Nowacek, D.P., Wasser, S.K., Kraus, S.D., 2012. Evidence that ship noise increases stress in right whales. Proc. Biol. Sci. 279, 2363–2368. URL. https://doi.org/10.1098/rspb.2011.2429.

Stapersma, D., Vrijdag, A., 2017. Linearisation of a ship propulsion system model. Ocean Eng. 142, 441–457. https://doi.org/10.1016/j.oceaneng.2017.07.014.

Tyack, P.L., 2008. Implications for marine mammals of large-scale changes in the marine acoustic environment. J. Mammal. 89 (3), 549–558. URL. https://dx.doi.org/10.1644/07-MAMM-S-307R.1.

van Terwisga, P.F., 2000. Hydrodynamic aspects of the application of a dynamic simulation model in frigate propulsion system design and operation. In: Proceedings of the 34th WEGEMT School.

van Terwisga, T.J.C., Noble, D.J., van 't Veer, R., Assenberg, F., McNeice, B., van Terwisga, P.F., August 8-13 2004. Effect of operational conditions on the cavitation inception speed of naval propellers. In: Proceedings of the 25th Symposium on Naval Hydrodynamics. Office of Naval Research, National Academies Pres, St. John's, Newfoundland and Labrador.

Verkuyl, J.B., van Terwisga, P.F., 2000. Testing a new fullscale cavitation observation system on board of Hr. Ms. Tydeman. In: Proceedings of the 34th WEGEMT School.

Vrijdag, A., Stapersma, D., 2017. Extension and application of a linearised ship propulsion system model. Ocean Eng. 143, 50–65. https://doi.org/10.1016/j.oceaneng.2017.07.023.

Vrijdag, A., Stapersma, D., Grimmelius, H., 2009. Control of propeller cavitation during a deceleration. In: Proceedings of the 14th Ship Control Systems Symposium. Ottawa, Canada.

Vrijdag, A., Stapersma, D., van Terwisga, T., 2010. Control of propeller cavitation in operational conditions. J. of Mar. Eng. and Technol. 9 (1), 15–26. https://doi.org/10.1080/20464177.2010.11020228.

Wesselink, A., Stapersma, D., van den Bosch, D., Teerhuis, P., March, 2006. Non-linear aspects of propeller pitch control. In: Proc. of the 2nd World Marit. Technology Conference (WMTC). IMarEST, London, isbn: 1-902536-54-1.

Glossary

Roman symbols

A: normalised propeller derivative[−]
B: normalised propeller derivative[−]
D: propeller diameter[m]
D: wake disturbance coefficient[−]
E: integral of the error[−]
E: Euler's number
E: normalised resistance steepness[−]
E: error[−]
F: force[N]
g: normalised engine derivative[−]
g: gravitational acceleration[$m{\cdot}s^{-2}$]
h: pressure coefficient[−]
I: polar moment of inertia[$kg{\cdot}m^{-2}$]
J: advance ratio[−]
K: coefficient[−]
K: wave number[$rad^2{\cdot}m^{-1}$]
K: gain[−]
M: torque[$N{\cdot}m$]
M: mass[kg]
n: rotation speed[rps]
p: pressure[Pa]
p: normalised propeller derivative[−]
Q: torque[$N{\cdot}m$]
q: normalised propeller derivative[−]
R: resistance[N]
T: thrust[$N{\cdot}m$]
t: time[s]
u: fluid velocity[$m{\cdot}s^{-1}$]
v: speed[$m{\cdot}s^{-1}$]
v: normalised engine derivative[−]
w: wake fraction[−]
X: fuel rack[mm]
Z: submergence[m]

Greek symbols

α: resistance factor[−]
ζ: sea surface elevation[−]
θ: propeller pitch angle[deg]
μ: heading relative to the waves[deg]
ρ: seawater density[$kg{\cdot}m^{-3}$]
σ: cavitation number[−]
τ: integration constant[s]
Φ: velocity potential[$m^2{\cdot}s^{-1}$]
Ω: wave frequency[$rad{\cdot}s^{-1}$]

Subscripts

0: nominal
a: advance
a: amplitude
a: atmosphere
b: brake
e: encounter
i: integral
n: shaft speed
p: polar
p: proportional
prop: propeller
Q: torque
s: ship
s: shaft
set: setpoint
T: thrust
v: ship speed
v: vapour
x: axial direction
θ: pitch